Supplementary Information for "Observation of topological prethermal strong zero modes"

CONTENTS

1. THEORETICAL ANALYSIS

In this section, we first analyze the 1D symmetry-protected topological (SPT) spin Hamiltonian and corresponding edge modes in the ground-state manifold. We explain why it is ruined by thermal excitations at finite temperatures, and how it presents as prethermal strong zero modes with dimerized parameters in the system Hamiltonian. Such strong zero modes can be understood as a consequence of U(1)×U(1) symmetry, which is approximately conserved in the system's prethermal regime. We introduce how to map our spin Hamiltonian into two Kitaev chains by applying the Jordan-Wigner transformation. In addition, we analyze the evolution circuit applied in our work, obtained from Trotterizing the Hamiltonian to the first-order. Finally, we explain how energy spectroscopy is carried out and the form of energy gaps in an integrable chain.

A. 1D SPT spin chain and edge modes at zero temperature

Our 1D Hamiltonian in the main text comprises two ingredients as $H = H_0(J_\mathrm{e}, J_\mathrm{o}) + H_1(h_x, V_{xx})$. The first part H_0 includes strong interaction among neighboring sites, which introduces SPT phases in our system. The second part H_1 considers perturbation terms, which include a transverse field in $\hat{x}$ direction and two-body XX interactions for neighboring qubits.

We first investigate the properties of the SPT Hamiltonian H_0:

$$H_0(J_\mathrm{e}, J_\mathrm{o}) = -J_\mathrm{e} \sum_{i=1}^{N/2-1} \sigma_{2i-1}^z \sigma_{2i}^x \sigma_{2i+1}^z - J_\mathrm{o} \sum_{i=1}^{N/2-1} \sigma_{2i}^z \sigma_{2i+1}^x \sigma_{2i+2}^z, \tag{S1}$$

which contains N qubits in total. In our study, we consider N to be an even number for simplicity of notation, while all results can readily be extended to odd-number cases. The Hamiltonian preserves a $\mathbb{Z}_2 \times \mathbb{Z}_2$ symmetry, which is generated by the parity operators on even sites $G_\mathrm{e} = \prod_{i=1}^{N/2} \sigma_{2i}^x$ and odd sites $G_\mathrm{o} = \prod_{i=1}^{N/2} \sigma_{2i-1}^x$. The three-body interacting terms $K_i = \sigma_{i-1}^z \sigma_i^x \sigma_{i+1}^z$ in H_0 commutes with each others and are called stabilizers. Note that there are only $N-2$ stabilizers in H_0, while the system degree of freedom is N. This leads to the system having a four-fold degenerate ground-state manifold. At zero temperature, the system stays in the ground states, which can be distinguished by two edge modes induced by the $\mathbb{Z}_2 \times \mathbb{Z}_2$ symmetry. To see this, first note that the parity operators can be decomposed into the product of stabilizers and operators at edges:

$$G_\mathrm{e} = \sigma_1^z \left(\prod_{i=1}^{N/2-1} K_{2i} \right) \sigma_{N-1}^z \sigma_N^x, \quad G_\mathrm{o} = \sigma_1^x \sigma_2^z \left(\prod_{i=1}^{N/2-1} K_{2i+1} \right) \sigma_N^z. \tag{S2}$$

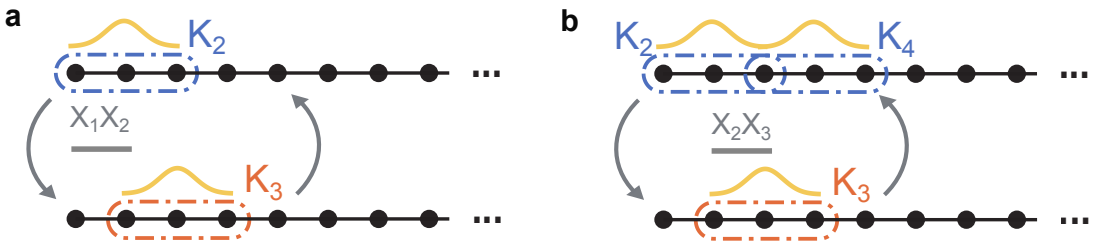

Fig. S1. **First-order resonances. a**, In the system with homogeneous stabilizer strength $J_o = J_e$, the two-body interaction $V_{xx}\sigma_1^x\sigma_2^x$ in H_1 can resonantly exchange one excitation between J_eK_2 and J_oK_3, which also flips $\tilde{Z}_L$ and $\tilde{X}_L$. **b**, In the system with stabilizer strength $J_o = 2J_e$, the $V_{xx}\sigma_2^x\sigma_3^x$ term resonantly transfers two excitations J_eK_2, J_eK_4 into J_oK_3, and vice versa. This process makes $\tilde{X}_L$ rapidly decohered. A similar process can happen at the right edge with $J_o = 0.5J_e$ and is not shown.

For ground states of H_0, all stabilizers K_i take constant values. In our case with positive J_e, J_o, all $K_i = 1$ in the ground states, leading to the parity operators further projected into the edges:

$$G_e = \sigma_1^z\left(\sigma_{N-1}^z\sigma_N^x\right) = \tilde{Z}_L\tilde{X}_R, \quad G_o = \left(\sigma_1^x\sigma_2^z\right)\sigma_N^z = \tilde{X}_L\tilde{Z}_R, \quad \begin{cases}\tilde{Z}_L \equiv \sigma_1^z\\ \tilde{X}_L \equiv \sigma_1^x\sigma_1^z\end{cases}, \quad \begin{cases}\tilde{Z}_R \equiv \sigma_N^z\\ \tilde{X}_R \equiv \sigma_{N-1}^z\sigma_N^x\end{cases}. \tag{S3}$$

As H_0 is local, the preserved symmetry $[H_0, G_e] = [H_0, \tilde{Z}_L\tilde{X}_R] = 0$ gives rise to both $[H_0, \tilde{Z}_L] = 0$ and $[H_0, \tilde{X}_R] = 0$. Similar results are obtained from $[H_0, G_o] = 0$, together gives four conserved quantities $\tilde{Z}_L$, $\tilde{X}_L$, $\tilde{Z}_R$, and $\tilde{X}_R$ at the edges. In addition, since $\tilde{Z}$ and $\tilde{X}$ are anti-commuted at both left and right edges, we conclude that the ground-state degeneracy is four-fold, with two effectively spin-1/2 edge modes described by $\tilde{Z}$ and $\tilde{X}$ residing at two ends of the chain. These edge operators connect between the different sectors of the ground-state manifold.

When generic perturbations are added into H_0, the $\mathbb{Z}_2 \times \mathbb{Z}_2$ symmetry is broken as the parity operators G_e, G_o are no longer preserved, destroying the edge modes. However, if the perturbations also preserve the $\mathbb{Z}_2 \times \mathbb{Z}_2$ symmetry with considerably small strength compared with the strength of stabilizers in H_0, which is the case in our work, the system remains deep in the SPT phase with the original localized edge modes now extend to the bulk of the system. These extensions make the left and right edge modes hybridize with each other, resulting in the original degenerated ground states now opening energy gaps $\zeta \propto \exp(-N)$ exponentially small in the system size. This gives rise to the exponentially long lifespan for edge modes at zero temperature under symmetry-preserved perturbations.

B. Edge modes as prethermal strong zero modes at finite temperatures

The above discussion is restricted to the system being in the ground state. At finite temperatures, thermal excitations emerge within the systems, interacting with edge modes and causing them to rapidly decohere. The vulnerability of edge modes against thermal excitations is uncovered by the fact that $\left(\prod_{i=1}^{N/2-1} K_{2i}\right)$ and $\left(\prod_{i=1}^{N/2-1} K_{2i+1}\right)$ in Eq. (S2) are no longer conserved quantities for excited states, and hence G_e, G_o cannot be projected into the edges. For example, for the perturbations in our work:

$$H_1(h_x, V_{xx}) = h_x\sum_{i=1}^{N}\sigma_i^x + V_{xx}\sum_{i=1}^{N-1}\sigma_i^x\sigma_{i+1}^x, \tag{S4}$$

directly applying $\sigma_1^x\sigma_2^x$ or considering the second-order process of $\sigma_1^x + \sigma_2^x$ will flip $\tilde{Z}_L$, $\tilde{X}_L$, K_2, and K_3, while keeping G_e and G_o unchanged. If exactly one of K_2 and K_3 is equal to -1, and both exhibit identical strength (i.e. $J_e = J_o$), this process further preserves the system energy and becomes a resonant perturbation, leading to rapid decoherence of both $\tilde{Z}_L$ and $\tilde{X}_L$. Physically, this represents transferring an excitation between the even and odd sites through the edge (Fig. S1a). Notably, the first-order resonance can happen at edges even for unequal stabilizer strength. For example, in the main text, we observe the left edge operator $\tilde{X}_L$ is rapidly decohered when $J_o/J_e = 2.0$. This is caused by the $\sigma_2^x\sigma_3^x$ term which flips $\tilde{X}_L$, K_2, K_3, and K_4, and hence resonantly transferring two excitations with energy J_e to one excitation with energy J_o (Fig. S1b). Similar process can happen for $\tilde{X}_R$ at right edge when $J_o/J_e = 0.5$. For systems taking other dimerized stabilizer strengths, the resonance only happens for higher-order processes that are hard to observe within the current experimental time scale. This leads to the prolonged edge mode lifetime observed in our experiment.

Theoretically, a local operator being approximately conserved for arbitrary system configurations is characterized by a prethermal strong zero mode (PSZM) [S1–S3]. Such an operator almost commutes with the system Hamiltonian and maps system eigenstates from one symmetry sector to another. By definition, a PSZM must satisfy the following three conditions: (1) Squares

to the identity. (2) Almost commutes with the Hamiltonian with an error term exponentially small in the system size. (3) Anti-commutes with the system's symmetry. In practice, such an operator is constructed from perturbation theory order by order and is cut off at some finite order to obtain a bounded commutator with the Hamiltonian. In our setting, the PSZM can be constructed for all $\tilde{Z}_{\mathrm{L}}$, $\tilde{X}_{\mathrm{L}}$, $\tilde{Z}_{\mathrm{R}}$, and $\tilde{X}_{\mathrm{R}}$, which leads to robust edge modes locally encoding spin-1/2 degrees of freedom at both ends of the chain under finite temperatures. Up to the first order in h_x and V_{xx}, such PSZMs for the left edge reads [S3],

$$\Psi_{\mathrm{L}}^{z} = \tilde{Z}_{\mathrm{L}} - \frac{h_x}{J_{\mathrm{e}}}\sigma_1^x\sigma_2^x\sigma_3^z + \frac{V_{xx}}{J_{\mathrm{o}}^2 - J_{\mathrm{e}}^2}(J_{\mathrm{e}}\sigma_1^x\sigma_3^z + J_{\mathrm{o}}\sigma_1^y\sigma_2^y\sigma_3^x\sigma_4^z), \tag{S5}$$

$$\begin{aligned}\Psi_{\mathrm{L}}^{x} = \tilde{X}_{\mathrm{L}} &- \frac{h_x}{J_{\mathrm{o}}}\sigma_1^x\sigma_2^x\sigma_3^x\sigma_4^z - \frac{V_{xx}}{J_{\mathrm{o}}^2 - J_{\mathrm{e}}^2}(J_{\mathrm{o}}\sigma_2^x\sigma_3^x\sigma_4^z + J_{\mathrm{e}}\sigma_1^z\sigma_2^z\sigma_3^z) \\ &+ \frac{V_{xx}J_{\mathrm{e}}}{J_{\mathrm{o}}^2 - 4J_{\mathrm{e}}^2}\left[\sigma_1^y\sigma_2^z\sigma_3^y + \left(\frac{2J_{\mathrm{e}}}{J_{\mathrm{o}}} - \frac{J_{\mathrm{o}}}{J_{\mathrm{e}}}\right)\sigma_1^x\sigma_2^x\sigma_4^z - \sigma_1^x\sigma_2^y\sigma_3^y\sigma_4^x\sigma_5^z - \frac{2J_{\mathrm{e}}}{J_{\mathrm{o}}}\sigma_1^y\sigma_4^y\sigma_5^z\right],\end{aligned} \tag{S6}$$

and similar PSZMs can be constructed for the right edge. We identify that both Ψ_{L}^z and Ψ_{L}^x commute with $H_0 + H_1$ and squares to the identity up to error terms with order $O\left(\max\{h_x^2, V_{xx}^2\}\right)$. For a homogeneous system with $J_{\mathrm{o}} = J_{\mathrm{e}}$, the first-order terms in both $\Psi_{\mathrm{L}}^z, \Psi_{\mathrm{R}}^x$ diverge, resulting from the resonant process of $V_{xx}\sigma_1^x\sigma_2^x$. In addition, we find Ψ_{L}^x also diverges at $J_{\mathrm{o}} = 2J_{\mathrm{e}}$, characterizing the effect of $V_{xx}\sigma_2^x\sigma_3^x$. Besides these divergent points, $\Psi_{\mathrm{L}}^z, \Psi_{\mathrm{R}}^x$ keep finite and satisfy $\{\Psi_{\mathrm{L}}^z, G_{\mathrm{o}}\} = [\Psi_{\mathrm{L}}^z, G_{\mathrm{e}}] = 0$ and $\{\Psi_{\mathrm{L}}^x, G_{\mathrm{e}}\} = [\Psi_{\mathrm{L}}^x, G_{\mathrm{o}}] = 0$. This induces the almost conserved degeneracy throughout the entire spectrum, thus giving rise to robust edge modes for arbitrary system configurations. Given that both h_x and V_{xx} remain small, Ψ_{L}^z and Ψ_{L}^x have large overlaps with $\tilde{Z}_{\mathrm{L}}$ and $\tilde{X}_{\mathrm{L}}$. This makes the latter operators, which we measure in experiments, good approximations to describe the edge modes.

C. Prethermalization and emergent U(1)×U(1) symmetry

It was recently shown in Ref. [S4] that PSZMs can be understood as a phenomenon of prethermalization with emergent symmetries. The authors proved that there was an additional U(1) symmetry in the prethermal regime of a Kitaev chain, given that the perturbations were much smaller than the interaction strength. This gave rise to robust Majorana edge modes at finite temperatures. For the SPT chain in our experiments, a similar U(1) symmetry is observed in the homogeneous regime (Fig. 3**d** in the main text), however, it is insufficient for protecting the spin-1/2 edge modes. Instead, we observe that the robust edge modes only occur under the protection of the U(1)×U(1) symmetry in the dimerized and off-resonant case.

We start with first investigating the emergent U(1) symmetry in the homogeneous case, which comes from considering the structure of the stabilizer terms in the Hamiltonian H. It has shown that after applying local Schrieffer-Wolff transformations order by order and stopping at a certain order to restrict the growth of perturbation terms, the symmetry-breaking perturbations can be eliminated in a rotated frame. In particular, if the system Hamiltonian takes the form

$$H = -JN + V, \tag{S7}$$

with N being a sum of mutual-commuting local terms and having integer eigenvalues, and V being a sum of local perturbations with energy scale J_0, the evolution generated by H can be approximated by the following equation [S5–S7]:

$$\exp(-iHt) = \mathcal{V}\exp\left[-i(-JN + V_p + E)t\right]\mathcal{V}^\dagger, \quad [N, V_p] = 0, \quad \|E\| = O\left[\exp\left(-\frac{J}{J_0}\right)\right]. \tag{S8}$$

Note that the system now preserves N up to an exponentially small error term E, indicating that an additional U(1) symmetry generated by N emerges. The system will eventually thermalize to an infinite-temperature state due to the errors E. However, before that, the effective Hamiltonian $-JN + V_p$ and the U(1) symmetry will survive for an exponentially long lifespan, referred to as the prethermal regime. In homogeneous system with $J_{\mathrm{e}} = J_{\mathrm{o}}$, the Hamiltonian $H = -J_{\mathrm{e}}\sum_{i=2}^{N-1} K_i + H_1(h_x, V_{xx})$ exactly fits into Eq. (S7). Given that $J_{\mathrm{e}} \gg \max\{h_x, V_{xx}\}$, the sum of stabilizers in bulk $\sum_{i=2}^{N-1} K_i$ is approximately conserved. This leads to the conservation law on the total excitation number $(N - 2 - \sum_{i=2}^{N-1} K_i)/2$, which generates the U(1) symmetry in the prethermal regime lasting for $t = O\left[\exp(J_{\mathrm{e}}/\max\{h_x, V_{xx}\})\right]$.

The edge mode of spin-1/2 fails to maintain robustness at finite temperatures, even in the presence of this additional U(1) symmetry. This is exemplified by the first-order resonant process depicted in Fig. S1**a**, where transferring an excitation between sites with different parity ruins the edge modes without modifying the total excitation number. The robust edge mode requires a larger symmetry group U(1)×U(1), denoting the conservation laws on excitation numbers within even and odd sites. Such a U(1)×U(1) symmetry can emerge within the system with dimerized stabilizer strength $J_{\mathrm{e}} \neq J_{\mathrm{o}}$. Intuitively, this separates the energy scales of stabilizers on the even and odd sites, leading to large energy obstacles on exchanging excitations. However, if the $J_{\mathrm{e}}/J_{\mathrm{o}}$ is a rational number, there could be resonant processes in the perturbation theory, which happens at a finite order

independent with J_o, J_e and the system size. The first-order resonance in the $J_o = 2J_e$ case is an example (Fig. S1**b**). To avoid these resonances, the stabilizer strength should be irrational multiples of each other. Then, the U(1)×U(1) symmetry is maintained within the exponentially long prethermal regime. Formally, for the Hamiltonian taking the form

$$H = -\sum_{i=1}^{m} J_i N_i + V, \tag{S9}$$

with $\{N_i\}$ be mutually commuting operators taking integer eigenvalues, and $\{J_i\}$ being irrational multiples of each other, and V being a sum of local perturbations with energy scale J_0, the evolution generated by H can be approximated by the following equation [S8]:

$$\exp(-iHt) = \mathcal{V}\exp\left[-i\left(-\sum_{i=1}^{m} J_i N_i + V_p + E\right)t\right]\mathcal{V}^\dagger, \quad \forall i,\ [N_i, V_p] = 0, \quad \|E\| = O\left[\exp\left(-\left(\frac{\min\{J_i\}}{J_0}\right)^{1/(m+\epsilon)}\right)\right], \tag{S10}$$

with ϵ being a small constant. Within the rotated frame $\mathcal{V}$, the system now presents m approximate conservation laws on all N_i, leading to the emergent $\mathrm{U}(1)^{\times m}$ symmetry. Note that for $m = 1$ the equation aligns with the one in Eq. (S8), and for our case with $m = 2$, the prethermal lifetime is proportional to $\exp\left[(\min\{J_e, J_o\}/\max\{h_x, V_{xx}\})^{1/2}\right]$.

The key point to understand how this emergent U(1)×U(1) symmetry gives rise to the robust edge modes is that the conserved sum of stabilizers on even and odd sites will also lead to the conserved parity of stabilizers on even and odd sites, i.e. $\prod_{i=1}^{N/2-1} K_{2i}$ and $\prod_{i=1}^{N/2-1} K_{2i+1}$, which are originally not conserved when there are thermal excitations in the homogeneous regime. With these conserved parity operators, together with the system preserved $\mathbb{Z}_2 \times \mathbb{Z}_2$ symmetry, we can again project G_e, G_o in Eq. (S2) into the edges and obtain Eq. (S3) without requiring the system being in ground states, leading to robust edge operators $\tilde{Z}, \tilde{X}$ for arbitrary system configurations.

D. Jordan-Wigner transformation and Majorana fermion picture

In the main text, we argue that our SPT qubit chain can be transformed into two Kitaev chains in the Majorana picture. To see this, we first consider applying the Jordan-Wigner transformation [S9] to map the spin Hamiltonian $H = H_0 + H_1$ into fermionic creation/annihilation operators $c_i^\dagger, c_i$:

$$\sigma_i^x = 1 - 2c_i^\dagger c_i, \quad \sigma_i^z = -\left[\prod_{j=1}^{i-1}(1 - 2c_j^\dagger c_j)\right](c_i^\dagger + c_i), \tag{S11}$$

and the inverse transformation is $c_i = -\frac{1}{2}\left(\prod_{j=1}^{i-1}\sigma_j^x\right)\sigma_i^z(1-\sigma_i^x)$, $c_i^\dagger = -\frac{1}{2}\left(\prod_{j=1}^{i-1}\sigma_j^x\right)(1-\sigma_i^x)\sigma_i^z$. This readily gives the canonical fermionic algebra $\{c_k, c_l^\dagger\} = \delta_{kl}, \{c_k, c_l\} = 0$. After applying Eq. (S11), H is transformed into the following form:

$$\begin{aligned} H_f = &-J_e\sum_{i=1}^{N/2-1}(c_{2i-1}^\dagger - c_{2i-1})(c_{2i+1}^\dagger + c_{2i+1}) - J_o\sum_{i=1}^{N/2-1}(c_{2i}^\dagger - c_{2i})(c_{2i}^\dagger + c_{2i}) + h_x\sum_{i=1}^{N}(1 - 2c_i^\dagger c_i) \\ &+V_{xx}\sum_{i=1}^{N-1}(1 - 2c_i^\dagger c_i)(1 - 2c_{i+1}^\dagger c_{i+1}) \end{aligned} \tag{S12}$$

$$\begin{aligned} = &\underbrace{\sum_{i=1}^{N/2-1}\left[-J_e(c_{2i-1}^\dagger - c_{2i-1})(c_{2i+1}^\dagger + c_{2i+1}) + h_x(1 - 2c_{2i-1}^\dagger c_{2i-1})\right] + h_x(1 - 2c_{N-1}^\dagger c_{N-1})}_{\text{Upper Kitaev chain}} \\ &+\underbrace{\sum_{i=1}^{N/2-1}\left[-J_o(c_{2i}^\dagger - c_{2i})(c_{2i+2}^\dagger + c_{2i+2}) + h_x(1 - 2c_{2i}^\dagger c_{2i})\right] + h_x(1 - 2c_N^\dagger c_N)}_{\text{Lower Kitaev chain}} \\ &+\underbrace{V_{xx}\sum_{i=1}^{N-1}(1 - 2c_i^\dagger c_i)(1 - 2c_{i+1}^\dagger c_{i+1})}_{\text{Inter-chain coupling}}. \end{aligned} \tag{S13}$$

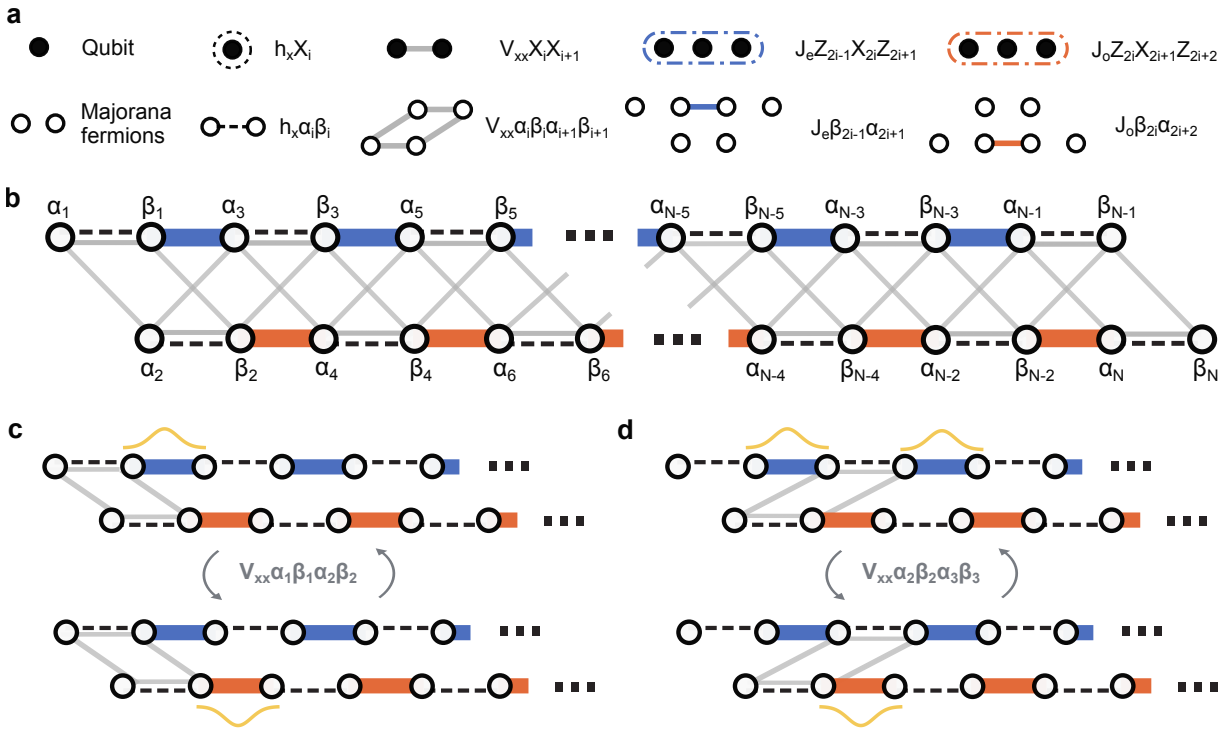

Fig. S2. **The SPT spin chain in the Majorana fermion picture. a,** The correspondence between each term in spin Hamiltonian H and Majorana operators α, β. Each qubit is non-locally transformed into two Majorana fermions. Single-body σ_i^x and two-body $\sigma_i^x\sigma_{i+1}^x$ terms are transformed into onsite and inter-chain couplings involving two and four Majoranas, respectively. The three-body stabilizers on even (odd) sites are mapped into couplings between two Majoranas on different sites. **b,** The SPT spin chain is transformed into two Kitaev chains with inter-site coupling strengths J_e (upper chain) and J_o (lower chain). **c-d,** The first-order resonances between two Kitaev chains for (c) $J_o = J_e$ and (d) $J_o = 2J_e$.

Here, we already obtain the result that the spin Hamiltonian is transformed into two Kitaev chains with distinct coupling strengths J_e and J_o, where onsite and inter-chain couplings are present with strengths h_x, V_{xx}, respectively. To see this result in the Majorana picture, we further transform each $c_i^\dagger, c_i$ into Majorana fermionic operators α_i, β_i by:

$$c_i^\dagger = \frac{\alpha_i - i\beta_i}{2}, \quad c_i = \frac{\alpha_i + i\beta_i}{2}. \tag{S14}$$

Then, the fermionic Hamiltonian in Eq. (S13) is mapped into:

$$H_{\rm mf} = \sum_{i=1}^{N/2-1} (iJ_e\beta_{2i-1}\alpha_{2i+1} - ih_x\alpha_{2i-1}\beta_{2i-1}) - ih_x\alpha_{N-1}^\dagger\beta_{N-1} + \sum_{i=1}^{N/2-1} (iJ_o\beta_{2i}\alpha_{2i+2} - ih_x\alpha_{2i}\beta_{2i}) - ih_x\alpha_N^\dagger\beta_N + V_{xx}\sum_{i=1}^{N-1}\alpha_i\beta_i\alpha_{i+1}\beta_{i+1}. \tag{S15}$$

In summary, the total transformation is given by

$$\sigma_i^x = -i\alpha_i\beta_i, \quad \sigma_i^z = -\left[\prod_{j=1}^{i-1}(-i\alpha_j\beta_j)\right]\alpha_i. \tag{S16}$$

We illustrate how each term in the spin Hamiltonian H mapped into Majorana fermionic operators in Fig. S2**a**, and the two coupled Kitaev chains after the transformation is shown in Fig. S2**b**.

A few remarks are in order. First, the edge operators originally defined in the spin Hamiltonian are now mapped into the following form:

$$\tilde{Z}_{\rm L} = -\alpha_1, \quad \tilde{X}_{\rm L} = -\alpha_2, \quad \tilde{Z}_{\rm R} = -i\left[\prod_{j=1}^{N}(-i\alpha_j\beta_j)\right]\beta_N, \quad \tilde{X}_{\rm R} = -i\left[\prod_{j=1}^{N}(-i\alpha_j\beta_j)\right]\beta_{N-1}. \tag{S17}$$

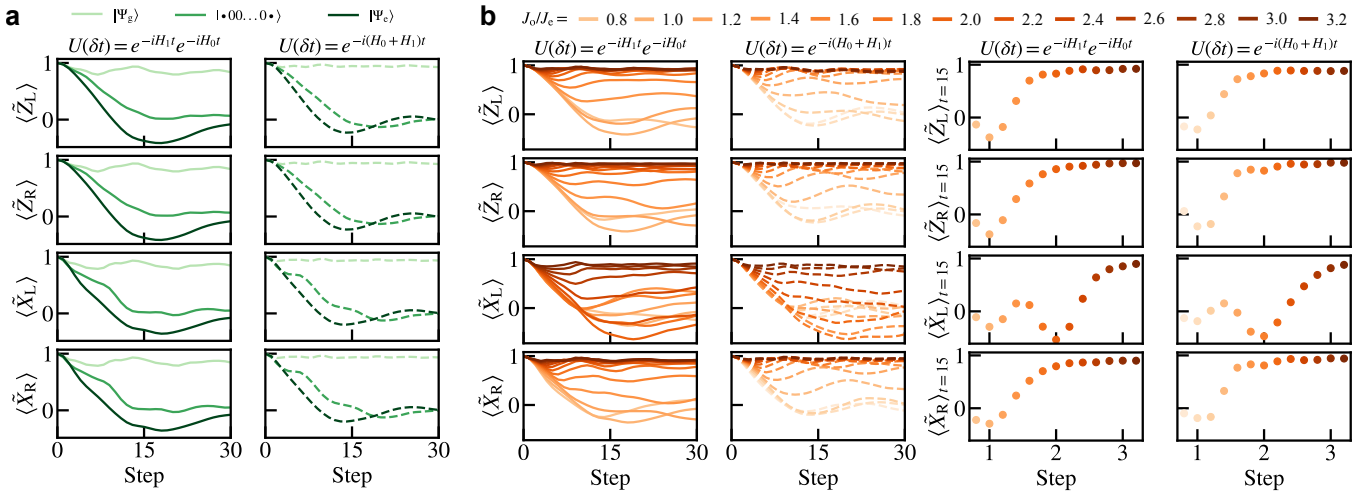

Fig. S3. **Comparison between the exact evolution and the evolution obtained from the first-order Trotterization. a,** Measured time dynamics for edge operators under the Trotter circuit (left) and the exact evolution (right) in the homogeneous regime ($J_o = J_e = \pi/5$). **b,** Measured time dynamics for edge operators with fixed $J_e = \pi/5$ and varying J_o. Data in the first (second) and third (fourth) columns are obtained from the Trotter circuit (exact evolution). The numerical calculations are carried out on a $N = 14$ system with $h_x = 0.11$ and $V_{xx} = 0.2$.

While the left edge operators are directly represented by Majorana edge modes α_1, α_2 in each Kitaev chain, there is an additional term $\prod_{j=1}^{N}(-i\alpha_j\beta_j)$ at right edges. Notably, this is the generator for the total $\mathbb{Z}_2$ symmetry:

$$G = \prod_{j=1}^{N}(-i\alpha_j\beta_j) = G_eG_o, \quad G_e = \prod_{i=1}^{N/2}(-i\alpha_{2i}\beta_{2i}), \quad G_o = \prod_{i=1}^{N/2}(-i\alpha_{2i-1}\beta_{2i-1}). \tag{S18}$$

As the system preserves G_e and G_o, it also preserves G. Therefore, the right edge operator $\tilde{Z}_R$, $\tilde{X}_R$ are sorely determined by the state of β_N, β_{N-1} during the evolution.

Second, the single-body and two-body terms in H_1 are mapped into onsite and inter-chain coupling terms. Given that h_x and V_{xx} are small, the system keeps in the topological phase with $\alpha_1, \alpha_2, \beta_{2N-1}, \beta_{2N}$ nearly unpaired. In addition, the first-order resonance we discussed above is better understood in the Majorana fermion picture. The $\sigma_1^x\sigma_2^x$ term now becomes $\alpha_1\beta_1\alpha_2\beta_2$, pairing α_1, α_2 and exchanging the occupation between $J_e\beta_1\alpha_3$ and $J_o\beta_2\alpha_4$ (Fig. S2**c**). The $\sigma_2^x\sigma_3^x$ term reads $\alpha_2\beta_2\alpha_3\beta_3$, which involves α_2 and transfers both occupied $J_e\beta_1\alpha_3$ and $J_e\beta_3\alpha_5$ into $J_o\beta_2\alpha_4$ (Fig. S2**d**). These readily give the first-order resonant conditions $J_o = J_e$ and $J_o = 2J_e$.

Third, in the Majorana picture, the U(1)×U(1) symmetry now represents the conservation laws for occupation numbers of inter-site couplings within each Kitaev chain, i.e. $\sum_{i=1}^{N-1}\beta_{2i-1}\alpha_{2i+1}$ and $\sum_{i=1}^{N-1}\beta_{2i}\alpha_{2i+2}$. As a result, the $\mathbb{Z}_2$ charges in the bulk of each chain are also conserved:

$$\mathcal{F}_o = \prod_{i=1}^{N/2-1}\beta_{2i-1}\alpha_{2i+1} = \beta_1\left(\prod_{i=2}^{N/2-1}\alpha_{2i-1}\beta_{2i-1}\right)\alpha_{N-1}, \quad \mathcal{F}_e = \prod_{i=1}^{N/2-1}\beta_{2i}\alpha_{2i+2} = \beta_2\left(\prod_{i=2}^{N/2-1}\alpha_{2i}\beta_{2i}\right)\alpha_N. \tag{S19}$$

As the U(1)×U(1) symmetry emerges in the dimerized and off-resonant region, the system commutes with all of the symmetries G_e, G_o, $\mathcal{F}_e$, and $\mathcal{F}_o$. This gives the conserved $\mathcal{F}_oG_o = (-i)^{N/2}\alpha_1\beta_{2N-1}$ and $\mathcal{F}_eG_e = (-i)^{N/2}\alpha_2\beta_{2N}$. Since α_1 (α_2) and β_{2N-1} (β_{2N}) are at two ends of the chain separated by N sites, and perturbations are local, we conclude that each of α_1, α_2, β_{2N-1} and β_{2N} is conserved.

E. Characterization of the evolution circuit

So far, our discussion has been focused on the system with Hamiltonian $H = H_0 + H_1$. Such a Hamiltonian is suitable for theoretical analysis, yet it poses considerable challenges for experimental implementation. This is due to the three-body interactions inherent in H_0, and the fact that H_0 and H_1 do not commute. We address this problem through digitally implementing the evolution of H_0, H_1 with duration δt by quantum circuits $U_0(\delta t)$, $U_1(\delta t)$. The evolution of $H_0 + H_1$ is then approximated by first-order Trotter decomposition $U(\delta t) = U_1(\delta t)U_0(\delta t)$. The robust edge modes in the dimerized regime can be observed

with the presence of these Trotter errors in our experiments. As shown in Fig. S3, we carry out the noiseless simulation on the temporal dependence of the edge modes under the Trottered circuit $e^{-iH_1\delta t}e^{-iH_0\delta t}$ and the exact evolution $e^{-i(H_0+H_1)\delta t}$. We observe that the behavior of edge modes are qualitatively similar in two cases, as they decay rapidly when the system is starting with finite-temperature states, and become resilient against excitations with dimerized J_o/J_e. Strikingly, the Trotter errors do not change the first-order resonance point at $J_o/J_e = 2$.

In addition, Trotter errors can be considered as additional perturbations added to the system, making the interactions between the edges and the bulk more general. To show this, We apply the Floquet-Magnus expansion [S10–S12] on the Trotter decomposition circuit U. Note that U is generated by the following time-dependent Hamiltonian:

$$H(t) = \begin{cases} 2H_0, & 0 < t \le \delta t/2, \\ 2H_1, & \delta t/2 < t \le \delta t. \end{cases}, \quad U(\delta t) = \mathcal{T} e^{-i\int_0^{\delta t} H(t)\mathrm{d}t} = e^{-i\delta t H_1} e^{-i\delta t H_0}. \tag{S20}$$

This is a Floquet process with periodicity δt. At the stroboscopic time $t = n\delta t$, the system evolution can be described by an effective Floquet Hamiltonian: $U(n\delta t) = \exp[-i(n\delta t)H_F]$. When H_0 and H_1 do not commute, H_F becomes non-local, which is constructed order by order through the Floquet-Magnus expansion:

$$H_F = \sum_{n=0}^{\infty} (\delta t)^n \Omega_n. \tag{S21}$$

This series expansion typically does not converge, potentially signaling the ergodicity of the Floquet process. However, given the scaling of the coefficient of the n-th order term proportional to $(\delta t)^n$, we expect that higher-order terms will not take effect until a considerable delayed time, provided that δt is relatively small. Consequently, truncating the series expansion after the first few orders usually suffices to depict the system behavior within an experimental timescale. In our scenario, the first two orders read,

$$\Omega_0 = \frac{1}{\delta t}\int_0^{\delta t} H(t_1)\mathrm{d}t_1 = H_0 + H_1, \tag{S22}$$

$$\begin{aligned} \Omega_1 &= \frac{1}{2i(\delta t)^2}\int_0^{\delta t}\mathrm{d}t_1\int_0^{t_1}\mathrm{d}t_2[H(t_1), H(t_2)] \\ &= -J_e h_x \sum_{i=1}^{N/2-1}\left(\sigma^y_{2i-1}\sigma^x_{2i}\sigma^z_{2i+1} + \sigma^z_{2i-1}\sigma^x_{2i}\sigma^y_{2i+1}\right) - J_o h_x \sum_{i=1}^{N/2-1}\left(\sigma^y_{2i}\sigma^x_{2i+1}\sigma^z_{2i+2} + \sigma^y_{2i}\sigma^x_{2i+1}\sigma^y_{2i+2}\right) \\ &\quad -J_e V_{xx}\left[\sum_{i=2}^{N/2-1}\sigma^x_{2i-2}\sigma^y_{2i-1}\sigma^x_{2i}\sigma^z_{2i+1} + \sum_{i=1}^{N/2-1}\left(\sigma^y_{2i-1}\sigma^z_{2i+1} + \sigma^z_{2i-1}\sigma^y_{2i+1} + \sigma^z_{2i-1}\sigma^x_{2i}\sigma^y_{2i+1}\sigma^x_{2i+2}\right)\right] \\ &\quad -J_o V_{xx}\left[\sum_{i=1}^{N/2-1}\left(\sigma^x_{2i-1}\sigma^y_{2i}\sigma^x_{2i+1}\sigma^z_{2i+2} + \sigma^y_{2i}\sigma^z_{2i+2} + \sigma^z_{2i}\sigma^y_{2i+2}\right) + \sum_{i=1}^{N/2-2}\sigma^z_{2i}\sigma^x_{2i+1}\sigma^y_{2i+2}\sigma^x_{2i+3}\right]. \end{aligned} \tag{S23}$$

This gives $H_F^{(2)} = H + (\delta t)\Omega_1$. Strikingly, besides H, additional interactions occur in $H_F^{(2)}$. As both H_0 and H_1 preserve the $\mathbb{Z}_2 \times \mathbb{Z}_2$ symmetry, Ω_1 also preserves it. Therefore, provided that δt is small, we expect $H_F^{(2)}$ with these additional perturbations will remain in the SPT phase.

F. Energy spectroscopy in an integrable chain

Here, we briefly explain how we measure the single-particle spectrum. First, we note that the Jordan-Wigner transformation in Eq. (S11) can also be applied to the quantum circuits in our experiments. In the limit with $V_{xx} = 0$, the unitary after transformation reads,

$$U_f = \left[\prod_{i=1}^{N/2-1} e^{i\delta t J_e(c^\dagger_{2i-1}-c_{2i-1})(c^\dagger_{2i+1}+c_{2i+1})}\prod_{i=1}^{N/2} e^{-i\delta t h_x(1-2c^\dagger_{2i-1}c_{2i-1})}\right]\left[\prod_{i=1}^{N/2-1} e^{i\delta t J_o(c^\dagger_{2i}-c_{2i})(c^\dagger_{2i+2}+c_{2i+2})}\prod_{i=1}^{N/2} e^{-i\delta t h_x(1-2c^\dagger_{2i}c_{2i})}\right] = U_{K,e}U_{K,o}, \tag{S24}$$

with mutually commuting $U_{\mathrm{K,e}}$ and $U_{\mathrm{K,o}}$. $U_{\mathrm{K,e}}$, $U_{\mathrm{K,o}}$, which are called kicked Kitaev models, are widely studied in theory [S13–S16]. This model is exactly solvable with Bogoliubov eigenmodes $\nu^\dagger, \nu$. For $U_{\mathrm{K,e}}$ and $U_{\mathrm{K,o}}$, we have

$$U_{\mathrm{K,e}}^\dagger \nu_{2i-1} U_{\mathrm{K,e}} = e^{-i\epsilon_{2i-1}} \nu_{2i-1}, \quad \nu_{2i-1} = \sum_{j=1}^{N/2} u_{2i-1,2j-1} c_{2j-1}^\dagger + v_{2i-1,2j-1} c_{2j-1}. \tag{S25}$$

$$U_{\mathrm{K,o}}^\dagger \nu_{2i} U_{\mathrm{K,o}} = e^{-i\epsilon_{2i}} \nu_{2i}, \qquad \nu_{2i} = \sum_{j=1}^{N/2} u_{2i,2j} c_{2j}^\dagger + v_{2i,2j} c_{2j}. \tag{S26}$$

$$\tag{S27}$$

Notably, as two kicked Kitaev chains are decoupled, the Bogoliubov eigenmodes are constructed from the fermionic operators within each chain, leading to

$$[U_{\mathrm{K,e}}, \nu_{2i}] = 0, \quad [U_{\mathrm{K,o}}, \nu_{2i-1}] = 0. \tag{S28}$$

In our experiments, we measure the logical operators $\tilde{Z}_{\mathrm{L}}, \tilde{Z}_{\mathrm{R}}$, which can be decomposed as following:

$$\tilde{Z}_{\mathrm{L}} = -(c_1 + c_1^\dagger) = \sum_{i=1}^{N/2} l_{2i-1} \nu_{2i-1} + l_{2i-1}^* \nu_{2i-1}^\dagger, \quad \tilde{Z}_{\mathrm{R}} = -G(c_N - c_N^\dagger) = G \sum_{i=1}^{N/2} l_{2i} \nu_{2i} + l_{2i}^* \nu_{2i}^\dagger. \tag{S29}$$

Again, we observe that the decomposition of $\tilde{Z}_{\mathrm{L}}$ ($\tilde{Z}_{\mathrm{R}}$) only involves the Bogoliubov eigenmodes within each Kitaev chain. Then, the dynamics of these operators from an arbitrary initial state $|\psi_0\rangle$ read

$$\langle\psi(t)|\tilde{Z}_{\mathrm{L}}|\psi(t)\rangle = \sum_{i=1}^{N/2} \left\langle \psi_0 \right| (U_{\mathrm{K,o}}^\dagger U_{\mathrm{K,e}}^\dagger)^t (l_{2i-1}\nu_{2i-1} + l_{2i-1}^* \nu_{2i-1}^\dagger)(U_{\mathrm{K,e}} U_{\mathrm{K,o}})^t \left| \psi_0 \right\rangle = \sum_{i=1}^{N/2} l_{2i-1} \langle\psi_0|\nu_{2i-1}|\psi_0\rangle e^{-it\epsilon_{2i-1}} + \text{h.c.}, \tag{S30}$$

$$\langle\psi(t)|\tilde{Z}_{\mathrm{R}}|\psi(t)\rangle = \sum_{i=1}^{N/2} \left\langle \psi_0 \right| (U_{\mathrm{K,o}}^\dagger U_{\mathrm{K,e}}^\dagger)^t G(l_{2i}\nu_{2i} + l_{2i}^* \nu_{2i}^\dagger)(U_{\mathrm{K,e}} U_{\mathrm{K,o}})^t \left| \psi_0 \right\rangle = \sum_{i=1}^{N/2} l_{2i} \langle\psi_0|G\nu_{2i}|\psi_0\rangle e^{-it\epsilon_{2i}} + \text{h.c.}, \tag{S31}$$

where h.c. denotes Hermitian conjugate terms. Provided that the initial state $|\psi_0\rangle$ has finite overlaps with each eigenmode ν, the Fourier transform of $\langle\psi(t)|\tilde{Z}_{\mathrm{L}}|\psi(t)\rangle$ ($\langle\psi(t)|\tilde{Z}_{\mathrm{R}}|\psi(t)\rangle$) reveals the spectrum $\{\epsilon_{2i-1}\}$ ($\{\epsilon_{2i}\}$) of the kicked Kitaev chain with inter-site coupling strength J_{e} (J_{o}). Consequently, their combination leads to the complete spectrum $\{\epsilon_1, \epsilon_2, \ldots, \epsilon_N\}$ of the system.

2. EXPERIMENTAL INFORMATION

A. Device performance

As shown in Fig. 1a of the main text, we construct a one-dimensional chain with 100 qubits on our 125-qubit quantum processor to implement the theoretical model. The wiring information for our device and room-temperature control electronics are sketched in Fig. S4. Figure S5a displays the idle frequencies of the 100 qubits, where we apply single-qubit gates in our experiments. The measured energy relaxation time T_1 and spin-echo dephasing time T_2^{SE} at idle frequencies in Fig. S5a are listed in Fig. S6, whose median values are 70.3 μs and 17.5 μs, respectively. Figure S5b shows the readout error for each qubit, which is defined by the average error of measuring $|0\rangle$ state and $|1\rangle$ state, which are measured by preparing the 100 qubits in random product states $\{|0\rangle, |1\rangle\}^{\otimes 100}$ and averaging for each qubit. We note that an extra microwave pulse that yields $|1\rangle \leftrightarrow |2\rangle$ transition is applied to each qubit before the readout microwave pulse to improve readout fidelity. The median value of readout errors is 0.88%.

B. Gate calibration

In our experiments, single-qubit gates are realized using 20-ns microwave pulses with Gaussian envelope modulated with the derivative reduction by adiabatic gate (DRAG) pulse. We compile consecutive single-qubit gates into a single-qubit rotation $U3(\theta, \varphi, \lambda)$ with the following matrix form

$$U3(\theta,\varphi,\lambda) = e^{-i\frac{\varphi}{2}\sigma_z} e^{-i\frac{\theta}{2}\sigma_y} e^{-i\frac{\lambda}{2}\sigma_z} = \begin{pmatrix} \cos\frac{\theta}{2} & -e^{i\lambda}\sin\frac{\theta}{2} \\ e^{i\varphi}\sin\frac{\theta}{2} & e^{i(\varphi+\lambda)}\cos\frac{\theta}{2} \end{pmatrix} \quad \text{(up to global phase)}. \tag{S32}$$

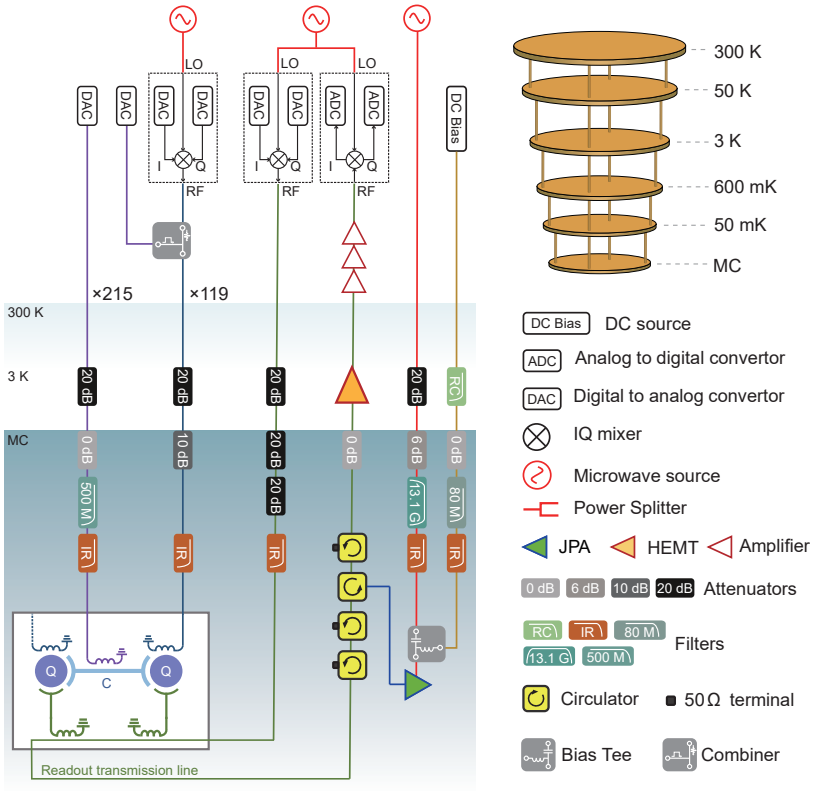

Fig. S4. **Experimental setup.** Quantum processor, denoted by the white box at the bottom left corner, is mounted on the mixing chamber plate (MC) of the dilution refrigerator, whose base temperature is around 20 mK. Fast Z-pulse lines (purple), microwave-drive lines (blue), and readout lines (green) connect room-temperature electronics to the processor for control and measurement. Details of the microwave components are provided in the legend on the right.

In practice, $U3(\theta, \varphi, \lambda)$ gate is realized by a virtual phase gate and a subsequent XY rotation. CPhase(ϕ) gates (ϕ is the conditional phase; $\phi \in \{\pi, -0.4\}$ in our experiments) are realized by tuning the $|11\rangle$ and $|20\rangle$ states of the two interacting qubits near resonance and switching on the coupling between them for a certain duration. Experimentally, we achieve a specific ϕ by tuning the Z-pulse amplitudes (amplitudes of the flux pulses input from fast Z-pulse lines in Fig. S4) of the qubits and coupler. The pulse durations for CZ and CPhase(-0.4) gates are 40 ns and 34 ns, respectively. As shown in Fig. S8, implementing a single Trotter step $U(\delta t)$ requires four layers of CZ gates, two layers of CPhase(-0.4) gates, and three layers of single-qubit gates, corresponding to a sequence of 288-ns duration, which places high demands on gate fidelity.

For CPhase(ϕ) gates with ϕ close to π (typically $|\phi - \pi| < 2$ in our case), we usually calibrate Z-pulse amplitudes of qubits either by maximizing qubit entanglement [S17] or Floquet calibration [S18, S19], and the Z-pulse amplitude of coupler is determined by minimizing leakage via measuring the probability of $|2\rangle$ state. While for the cases of $|\phi - \pi| \geq 2$, the low-leakage area becomes broad, making it hard to identify the right parameters [S20]. Here, we propose a sequence to calibrate CPhase gates with arbitrary conditional phase ϕ (Fig. S7), which we use to calibrate the Z-pulse amplitudes of qubits for CZ gates. Specifically, for CPhase(-0.4) gates, we start from the control parameters of CZ gates and use Floquet calibration to initialize the Z-pulse amplitudes of qubits so that the conditional phase is around 4.5. Then, we use the sequence described in Fig. S7 to calibrate the Z-pulse amplitude of the coupler.

C. Experiment circuits

In this section, we illustrate details about the main quantum circuits used in our experiments. Figure S8a and b show the quantum circuit for measuring $\tilde{Z}$ and $\tilde{X}$ operators in Fig. 2 and Fig. 3 of the main text at $t = 1$ (circuits with $t > 1$ are constructed by repeating the Trotter step circuit). In the experimental realization, the circuit will be further compiled to reduce the circuit depth. For example, the excitation gate $X(\pi)$ acting on Q_i in Fig. S8a is compiled as three gates $\{Z(\pi), X(\pi), Z(\pi)\}$ acting on $\{Q_{i-1}, Q_i, Q_{i+1}\}$ before the first layer of CZ gates. Then, these gates are merged into the Hadamard gate layer. Further, the CZ layers surrounded by the orange dashed frame in Fig. S8a are eliminated because the two CZ gates on edges are redundant (edge

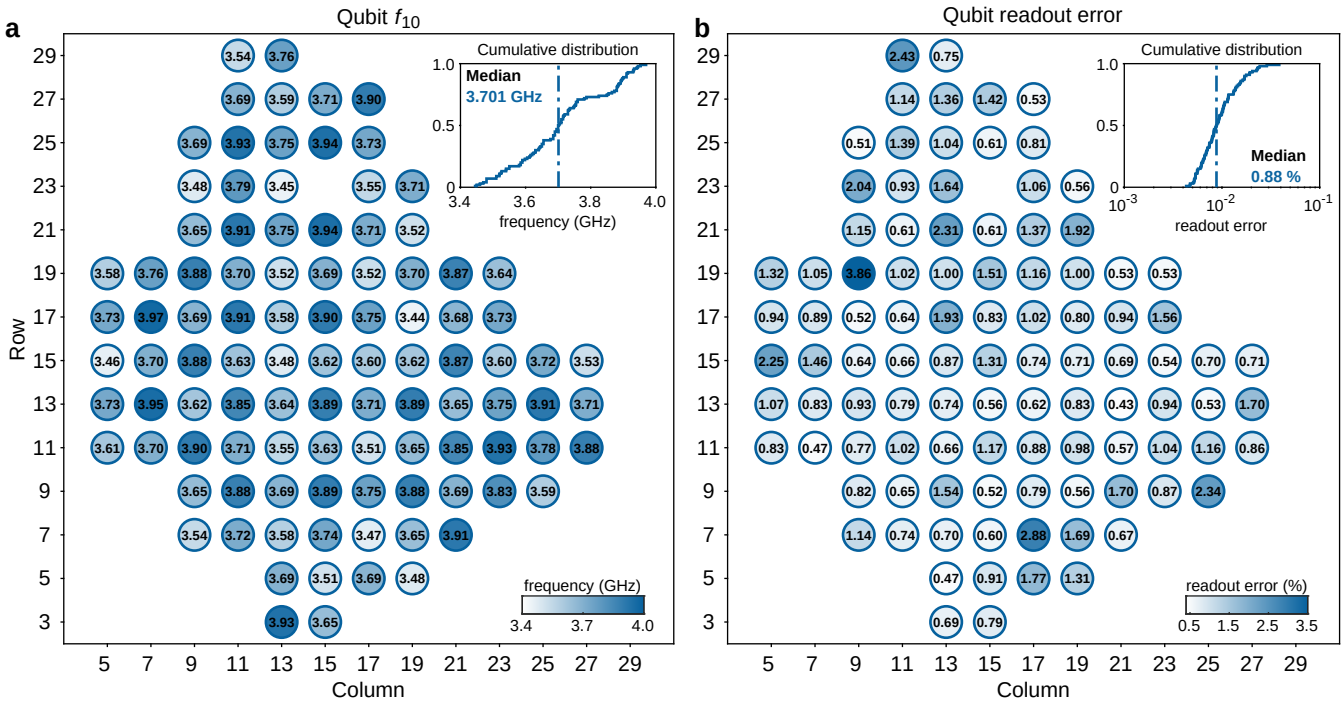

Fig. S5. **Qubit idle frequency and readout error. a**, Idle frequencies for all 100 qubits used in our experiments. Inset shows the cumulative distribution, with the dashed line indicating the median value. **b**, Qubit readout errors measured at idle frequencies in **a**. The data for each qubit is the average of the errors when qubit in state $|0\rangle$ and $|1\rangle$.

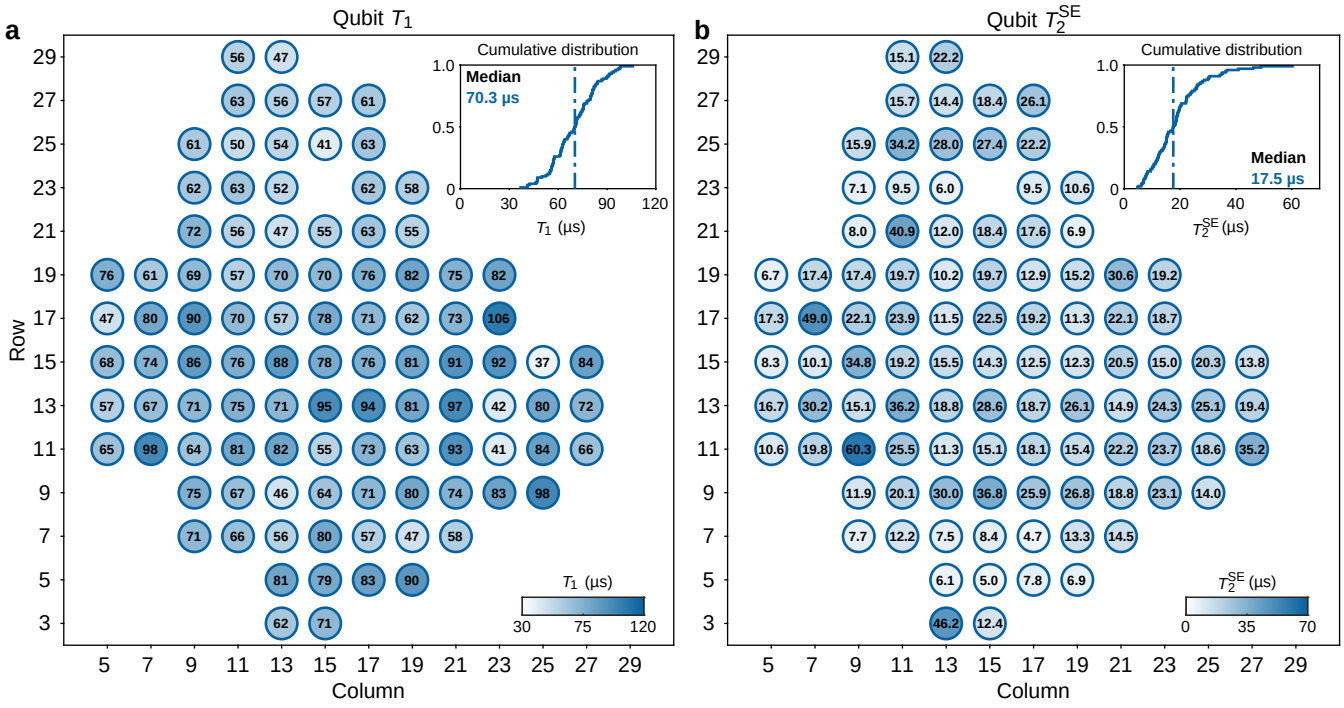

Fig. S6. **Qubit coherence time. a**, Energy relaxation time T_1 of the 100 qubits measured at idle frequencies, with a median value of 70.3 μs. **b**, Spin-echo dephasing time measured at idle frequencies, with a median value of 17.5 μs.

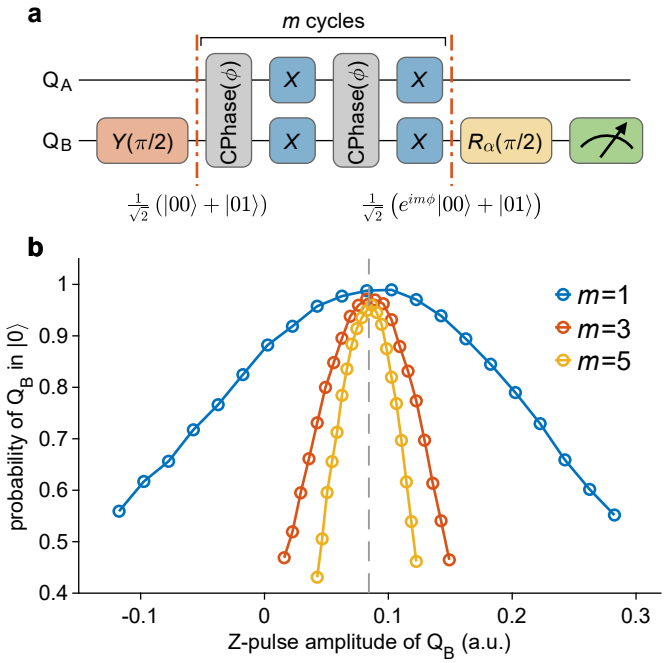

Fig. S7. **CPhase gate calibration.** **a**, Quantum circuit for calibrating CPhase(ϕ) gate. The circuit begins with a $Y(\pi/2)$ gate acting on Q_B, which prepares a superposition state $(|00\rangle + |01\rangle)/\sqrt{2}$. Then, m cycles of the interleaved circuit (including two layers of CPhase(ϕ) gates and two layers of single-qubit X gates) are applied, with each cycle accumulating a phase of ϕ on $|00\rangle$ state. Finally, an $R_\alpha(\pi/2)$ gate (a single-qubit rotation around the α-axis of Bloch sphere, where α refers to an equatorial rotation axis that has an angle α with respect to the x-axis) is applied to Q_B before readout. The measured probability of Q_B in $|0\rangle$ state is given by $[1 + \cos(\pi/2 + \alpha + m\phi)]/2$. In the ideal case without errors, by choosing $\alpha = -m\phi - \pi/2$, we should expect Q_B to be in $|0\rangle$ state with probability of 1. **b**, Measured probability of Q_B in $|0\rangle$ state as a function of the Z-pulse amplitude of Q_B. Gray dashed line indicates the calibrated Z-pulse amplitude we choose for Q_B.

qubits are in $|0\rangle$ state) and the rest CZ gates in the bulk can cancel out with each other. This similar elimination is also applied to the circuit in Fig. S8b as well. Note that the two-qubit gates in Trotter steps of $t > 1$ can not be eliminated.

After compilation, we utilize the Pauli twirling technique to suppress the damaging coherent noise, which is realized by inserting random single-qubit gates before and after each two adjacent CZ layers. To protect the edge qubits from dephasing noise, we also impose the restriction that a π-rotation is always embedded in the single-qubit layer that is sandwiched by the four CZ layers for the two edge qubits.

The echo evolution $U_{\text{echo}}(t) = (U^\dagger)^t U^t$ in the main text consists of t steps of forward time evolution U^t and the followed t steps of backward time evolution $(U^\dagger)^t$. Thus, the decay of echo evolution characterizes the accumulated circuit errors after initial state preparation. In our experiments, the circuit of U^t is defined as the circuit after the green dashed line in Fig. S8, where the Pauli twirling gates are also integrated.

D. Mitigation of leakage error

The experimental circuit for measuring the energy spectrum in Fig. 4 of the main text contains up to 150 Trotter steps with 900 layers of two-qubit gates. Such a long sequence makes the leakage to $|2\rangle$ state non-negligible, which systematically causes a slightly higher probability of qubit in $|1\rangle$ state. To suppress this effect, we also measure the $|2\rangle$ state probability in the many-body spectroscopy experiment and correct the experimental data with the following procedure.

- First, we run the experimental circuits and measure the probability of the qubit $\vec{P}_{\text{exp}} = \left(p_{0,\text{exp}}, p_{1,\text{exp}}, p_{2,\text{exp}}\right)^{\text{T}}$, where $p_{\alpha,\text{exp}}$ is the measured probability of qubit in $|\alpha\rangle$ state ($\alpha \in \{0, 1, 2\}$).
- Then, we use three-level readout correction matrix C to mitigate readout errors, which satisfies $C\vec{P}_{\text{ideal}} = \vec{P}_{\text{exp}}$ with the definition as below

$$C = \begin{pmatrix} 1 - \epsilon_{0\to1} - \epsilon_{0\to2} & \epsilon_{1\to0} & \epsilon_{2\to0} \\ \epsilon_{0\to1} & 1 - \epsilon_{1\to0} - \epsilon_{1\to2} & \epsilon_{2\to1} \\ \epsilon_{0\to2} & \epsilon_{1\to2} & 1 - \epsilon_{2\to0} - \epsilon_{2\to1} \end{pmatrix}, \tag{S33}$$

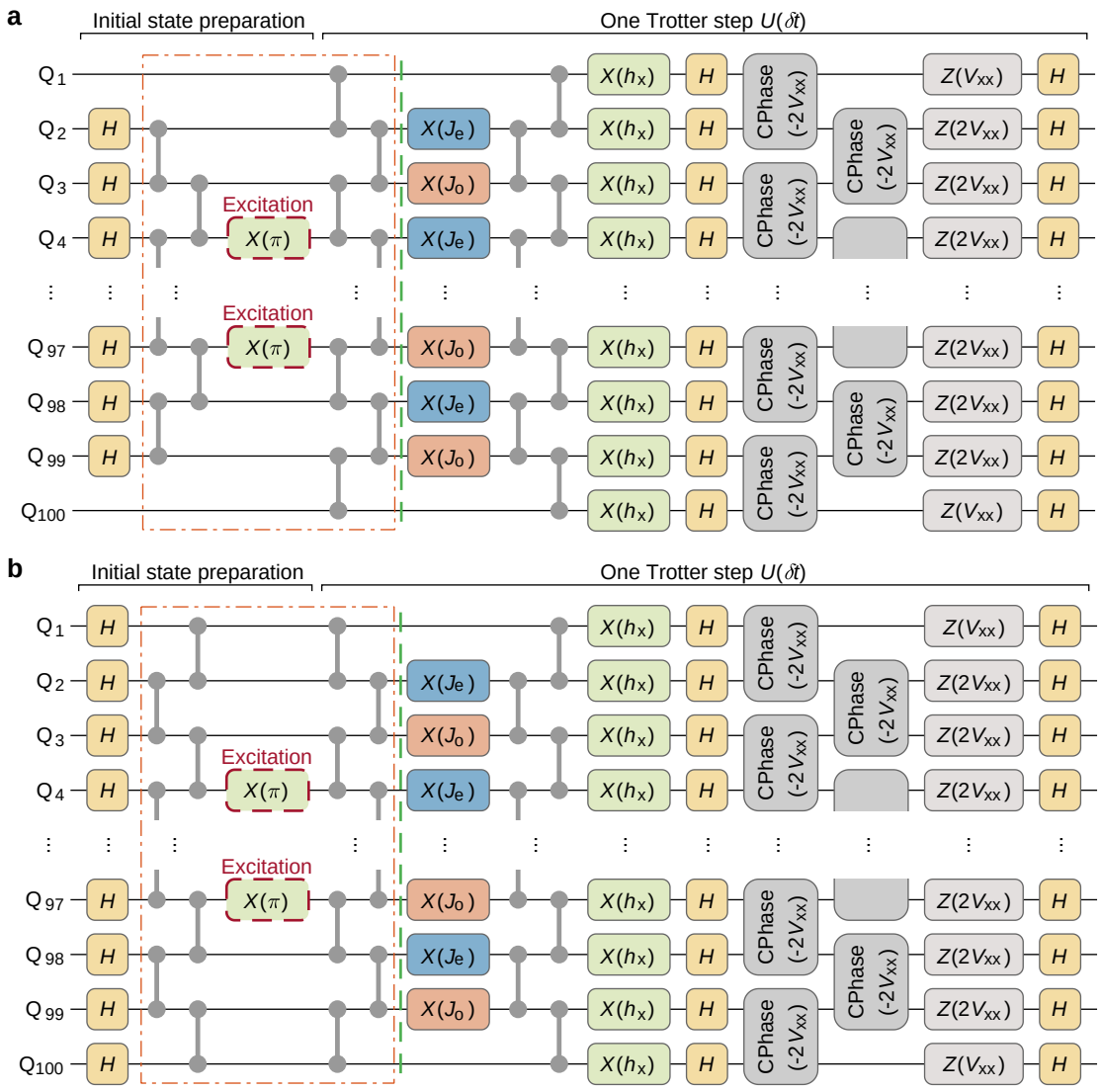

Fig. S8. **Experimental circuits.** **a**, Quantum circuit for measuring $\tilde{Z}$ operator in Fig. 2 of the main text when $t = 1$. The CZ gates in the orange dashed frame are canceled out after compilation in our experiments. The circuit on the right of the green dashed line corresponds to the unitary U^t as the building block of the echo circuit $U_{\text{echo}}(t) = (U^\dagger)^t U^t$. **b**, Quantum circuit for measuring $\tilde{X}$ operator in Fig. 2 and Fig. 3 of the main text when $t = 1$.

where $\epsilon_{i\to j}$ refers to the measured probability of a qubit in $|j\rangle$ when it is prepared in $|i\rangle$ state. The matrix elements of C are benchmarked with a separate experiment. Thus, the estimated $\vec{P}_{\text{ideal}}$ after readout correction is given by $\vec{P}_{\text{corr}} = C_{\text{exp}}^{-1}\vec{P}_{\text{exp}}$, where C_{exp}^{-1} is experimentally measured readout correction matrix.

- To eliminate the state leakage error, we discard the probability in $|2\rangle$ state and normalize the measured probability in the computational space with the following equation

$$p_{0,\text{norm}} = \frac{p_{0,\text{corr}}}{p_{0,\text{corr}} + p_{1,\text{corr}}}, p_{1,\text{norm}} = \frac{p_{1,\text{corr}}}{p_{0,\text{corr}} + p_{1,\text{corr}}}. \tag{S34}$$

- Finally, we calculate the expectation value $\langle\tilde{Z}\rangle = p_{0,\text{norm}} - p_{1,\text{norm}}$. In Extended Data Fig. 4, we show three representative time-domain signals of the measured $\langle\tilde{Z}_L\rangle$ and $\langle\tilde{Z}_R\rangle$.

E. Quantum state tomography

In this section, we provide details about how we obtain the density matrix in the main text. To investigate the dynamics of logical state fidelity (Fig. 5a of the main text), it is natural to perform two-qubit logical state tomography on the two edge states and reconstruct the full logical density matrix ρ_{logic}, then calculate the logical state fidelity $F\left(\rho_{\text{logic}}, \rho_{\text{ideal}}\right)$ (ρ_{ideal} is the ideal density matrix of logical state) by the following formula

$$\rho_{\text{logic}} = \frac{1}{4}\left(\sum_{\tilde{P}_{\text{L}},\tilde{P}_{\text{R}}\in\{I,\tilde{X},\tilde{Y},\tilde{Z}\}} \langle \tilde{P}_{\text{L}}\tilde{P}_{\text{R}}\rangle\, \tilde{P}_{\text{L}}\tilde{P}_{\text{R}}\right), \tag{S35}$$

$$F\left(\rho_{\text{logic}}, \rho_{\text{ideal}}\right) = \text{tr}\left(\sqrt{\sqrt{\rho_{\text{logic}}}\rho_{\text{ideal}}\sqrt{\rho_{\text{logic}}}}\right)^2, \tag{S36}$$

where $\tilde{X}, \tilde{Y}, \tilde{Z}$ are logical Pauli operators. To obtain the fidelity of logical Bell state $(|\tilde{0}\rangle_{\text{L}}|\tilde{0}\rangle_{\text{R}} + \text{i}|\tilde{1}\rangle_{\text{L}}|\tilde{1}\rangle_{\text{R}})$ in Fig. 5a of the main text, we simplify the measurement of $F\left(\rho_{\text{logic}}, \rho_{\text{ideal}}\right)$ by only probing three logical Pauli strings

$$F_{\text{Bell}} = \frac{1}{4}\left(1 + \langle \tilde{X}_{\text{L}}\tilde{Y}_{\text{R}}\rangle + \langle \tilde{Y}_{\text{L}}\tilde{X}_{\text{R}}\rangle + \langle \tilde{Z}_{\text{L}}\tilde{Z}_{\text{R}}\rangle\right). \tag{S37}$$

However, in Fig. 5b of the main text and Extended Data Fig. 5b, we measure all the logical Pauli operators in Eq. S35 to reconstruct all the elements of the full density matrices. In Extended Data Fig. 5c, we perform full quantum state tomography of the four physical qubits $Q_1, Q_2, Q_{99}, Q_{100}$ at edges and reconstruct its density matrix with a similar method of Eq. S35. The reconstructed full density matrices are further validated in the constraints of Hermitian, unit trace, and positive semi-definite with the method described in Ref. [S21].

[S1] Fendley, P. Strong zero modes and eigenstate phase transitions in the XYZ/interacting Majorana chain. *J. Phys. A: Math. Theor.* **49**, 30LT01 (2016).

[S2] Kemp, J., Yao, N. Y., Laumann, C. R. & Fendley, P. Long coherence times for edge spins. *J. Stat. Mech.* **2017**, 063105 (2017).

[S3] Kemp, J., Yao, N. Y. & Laumann, C. R. Symmetry-enhanced boundary qubits at infinite temperature. *Phys. Rev. Lett.* **125**, 200506 (2020).

[S4] Else, D. V., Bauer, B. & Nayak, C. Prethermal phases of matter protected by time-translation symmetry. *Phys. Rev. X* **7**, 011026 (2017).

[S5] Abanin, D., Roeck, W. D., Ho, W. W. & Huveneers, F. A rigorous theory of many-body prethermalization for periodically driven and closed quantum systems. *Commun. Math. Phys.* **354**, 809–827 (2017).

[S6] Else, D. V., Fendley, P., Kemp, J. & Nayak, C. Prethermal strong zero modes and topological qubits. *Phys. Rev. X* **7**, 041062 (2017).

[S7] Machado, F., Else, D. V., Kahanamoku-Meyer, G. D., Nayak, C. & Yao, N. Y. Long-range prethermal phases of nonequilibrium matter. *Phys. Rev. X* **10**, 011043 (2020).

[S8] Else, D. V., Ho, W. W. & Dumitrescu, P. T. Long-lived interacting phases of matter protected by multiple time-translation symmetries in quasiperiodically driven systems. *Phys. Rev. X* **10**, 021032 (2020).

[S9] Lieb, E., Schultz, T. & Mattis, D. Two soluble models of an antiferromagnetic chain. *Ann. Phys.* **16**, 407–466 (1961).

[S10] Magnus, W. On the exponential solution of differential equations for a linear operator. *Commun. Pure Appl. Math.* **7**, 649–673 (1954).

[S11] Kuwahara, T., Mori, T. & Saito, K. Floquet–Magnus theory and generic transient dynamics in periodically driven many-body quantum systems. *Ann. Phys.* **367**, 96–124 (2016).

[S12] Heyl, M., Hauke, P. & Zoller, P. Quantum localization bounds Trotter errors in digital quantum simulation. *Sci. Adv.* **5**, eaau8342 (2019).

[S13] Thakurathi, M., Patel, A. A., Sen, D. & Dutta, A. Floquet generation of Majorana end modes and topological invariants. *Phys. Rev. B* **88**, 155133 (2013).

[S14] Akila, M., Waltner, D., Gutkin, B. & Guhr, T. Particle-time duality in the kicked Ising spin chain. *J. Phys. A: Math. Theor.* **49**, 375101 (2016).

[S15] Bertini, B., Kos, P. & Prosen, T. Exact spectral form factor in a minimal model of many-body quantum chaos. *Phys. Rev. Lett.* **121**, 264101 (2018).

[S16] Lerose, A., Sonner, M. & Abanin, D. A. Scaling of temporal entanglement in proximity to integrability. *Phys. Rev. B* **104**, 035137 (2021).

[S17] Ren, W. *et al.* Experimental quantum adversarial learning with programmable superconducting qubits. *Nat. Comput. Sci.* **2**, 711–717 (2022).

[S18] Neill, C. *et al.* Accurately computing the electronic properties of a quantum ring. *Nature* **594**, 508–512 (2021).

[S19] Mi, X. *et al.* Time-crystalline eigenstate order on a quantum processor. *Nature* **601**, 531–536 (2022).

[S20] Foxen, B. *et al.* Demonstrating a continuous set of two-qubit gates for near-term quantum algorithms. *Phys. Rev. Lett.* **125**, 120504 (2020).

[S21] Smolin, J. A., Gambetta, J. M. & Smith, G. Efficient method for computing the maximum-likelihood quantum state from measurements with additive gaussian noise. *Phys. Rev. Lett.* **108**, 070502 (2012).